Supplement of Atmos. Chem. Phys., 20, 10351–10377, 2020
https://doi.org/10.5194/acp-20-10351-2020-supplement

Supplement of

Treatment of non-ideality in the SPACCIM multiphase model – Part 2: Impacts on the multiphase chemical processing in deliquesced aerosol particles

Ahmad Jhony Rusumdar et al.

Correspondence to: Ralf Wolke (wolke@tropos.de) and Hartmut Herrmann (herrmann@tropos.de)

Supplement S1: Additional material to section 3.5

C_3 organic chemistry results

As presented in former CAPRAM studies (e.g. Tilgner and Herrmann (2010)), methylglyoxal is effectively oxidised under cloud conditions, leading to the formation of substituted C_3 carboxylic acids, which are expected to be further oxidised in aqueous aerosols. In Fig. S1, the aqueous-phase concentrations of the main C_3 oxidation products, such as pyruvic acid, 3-oxo pyruvic acid, and finally keto malonic acid, along with corresponding activity coefficients are plotted throughout the simulation time for all urban scenarios. The corresponding plots for the remote scenario are presented in Fig. S14.

Figure S1 shows that the first stage oxidation product, pyruvic acid, is effectively produced under both day- and nighttime cloud conditions. Noticeably, urban nighttime clouds reveal a higher production of pyruvic acid than corresponding daytime clouds. This finding is in agreement with former studies (Tilgner and Herrmann, 2010; Tilgner et al., 2013), showing that in-cloud NO_3 radical oxidation represents an important sink for methylglyoxal and, consequently, a source for pyruvic acid under urban conditions.

Figure S1 illustrates that the activity coefficients of formed oxidation products are below unity for their dissociated forms in the 90 %-NIDU and 70 %-NIDU simulations under deliquesced aerosol conditions. However, their undissociated forms partly show activity coefficients above unity. Consequently, the non-ideality treatment can affect their further chemical processing differently in addition to the affected oxidant budget. In detail, undissociated pyruvic acid is characterised by activity coefficients above unity (about 1.5 in the 90 %-NIDU case) and its dissociated form by values of about 0.4 (90 %-NIDU case). Thus, non-ideality effects can increase the chemical processing of pyruvic acid and decrease the chemical processing of pyruvate. Under 70 %-NIDU conditions, pyruvic acid and pyruvate are characterised by even more different activity coefficients of about 3.0 and 0.3, respectively. Therefore, even higher differences between the ideal and the non-ideal treatment can occur.

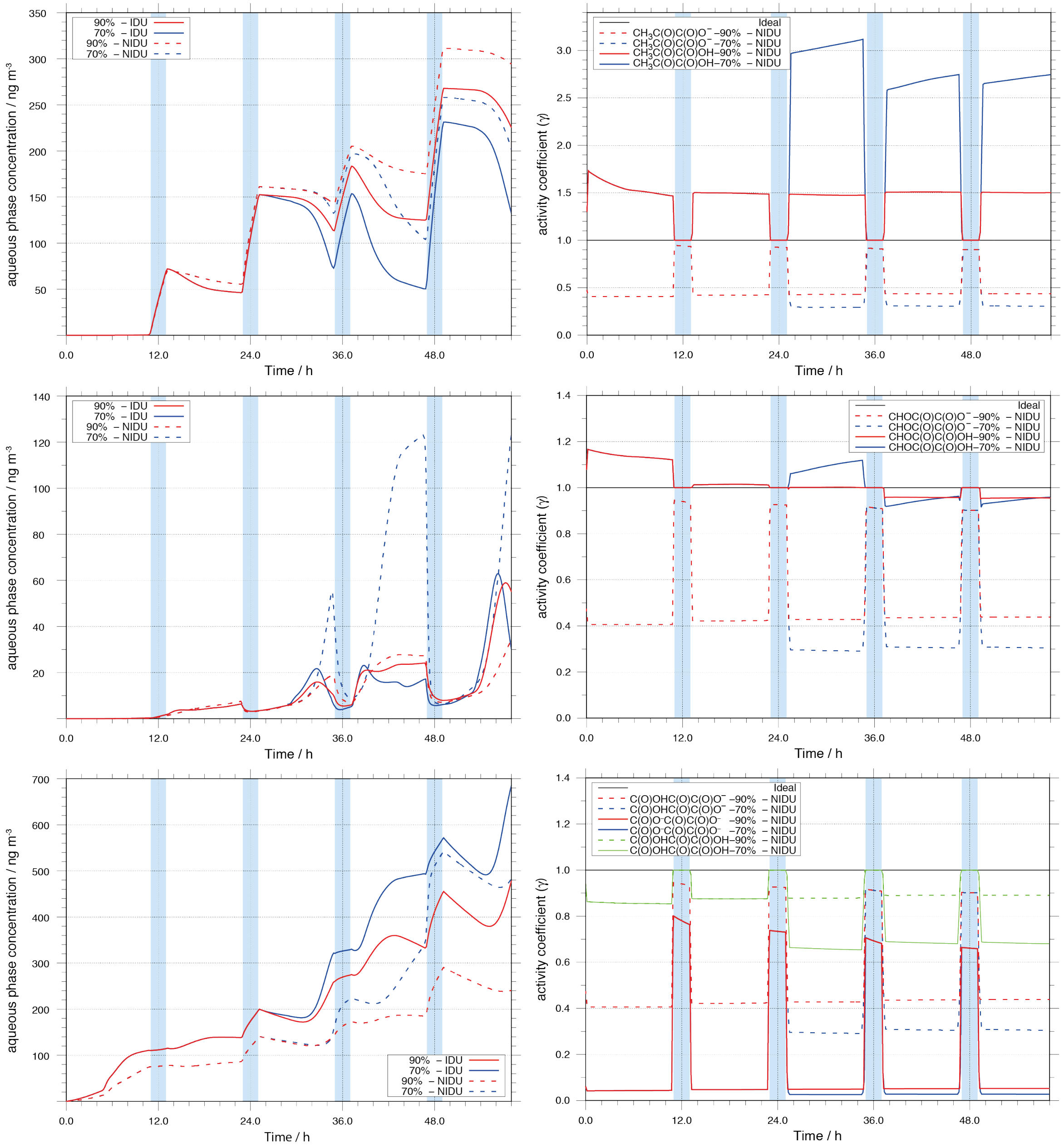

Figure S1 Modelled aqueous-phase concentrations in ng m$^{-3}{}_{\text{(air)}}$ and corresponding activity coefficients for the important C$_3$ oxidation products, (i) pyruvic acid (top), (ii) 3-oxo-pyruvic acid (centre), and (iii) keto malonic acid (down). The plotted concentrations represent the sum of dissociated and undissociated forms of the carboxylic acids.

5 Figure S1 shows that the in-cloud formations of pyruvic acid and keto malonic acid are similar in the 90 %-NIDU and 90 %-IDU cases. Differences between predicted concentration curves arise mainly during deliquesced aerosol periods. For pyruvic

acid, the ideal simulation is characterised by a faster degradation during aqueous aerosol conditions. In contrast, the 90 %-NIDU case shows a much lower decrease. This lower oxidation rate leads to the higher concentrations of pyruvic acid in the 90 %-NIDU case than in the 90 %-IDU case. Interestingly, Fig. S1 illustrates that the decrease is lower in the 90 %-NIDU case but higher under 70 %-NIDU conditions. A comparison of the 90 %-NIDU vs. 70 %-NIDU concentration profiles shows a stronger oxidation in the more concentrated solution case in the afternoon and evening of the second model day. Therefore, lower pyruvic acid concentrations and, consequently, higher 3-oxo pyruvic acid concentrations can be found in the 70 %-NIDU simulation during this period. The reasons for these higher oxidation levels in the aerosol phase of the 70 %-NIDU case are (i) the higher OH budget in the 70 %-NIDU case (see Sect. 3.3) and (ii) the substantially higher activity coefficients of pyruvic acid under 70 % RH conditions, which leads to faster degradation. A reaction rate investigation of OH radicals has already revealed the higher degradation rates of pyruvic acid under lower humidity conditions (see Sect. 3.3). An analysis of the reaction rates of pyruvic acid reveals degradation rates that are a factor of 2.7 higher in the 70 %-NIDU than in the 90 %-NIDU case during the aerosol period of 37-47 h.

Subsequently, further oxidation of 3-oxo pyruvic acid mainly occurs during cloud periods and leads to the formation of keto malonic acid (see Fig. S2). Keto malonic acid is the C_3 oxidation product of this oxidation chain, which is formed particularly under cloud and daytime deliquesced particle conditions. Due to the non-ideality treatment, the predicted concentrations of keto malonic acid are lower when compared to the ideal cases. The predicted concentration of keto malonic acid at the end of the 90 %-NIDU simulation is a factor of 2 lower.

From Fig. S2, it can be seen that the generally lowered oxidation of the precursors leads to a smaller production of keto malonic acid. On the other hand, the lowered oxidation of keto malonic acid compensates for the lowered formation rates. In detail, both the total keto malonic acid formation and sink rates are approximately 50 % lower in the 90 %-NIDU compared to the 90 %-IDU case throughout the whole simulation time. This interplay causes the relatively small differences in the predicted concentrations modelled between the ideal and non-ideal cases. Furthermore, Fig. S2 shows that both the formation patterns change in a way that makes keto malonic acid show less chemical aerosol phase rates and more distinct in-cloud rates. This means that the non-ideality treatment could both decrease (e.g. in 90 %-NIDU) and increase (e.g. in 70 %-NIDU) the chemical turnovers in the aerosol phase.

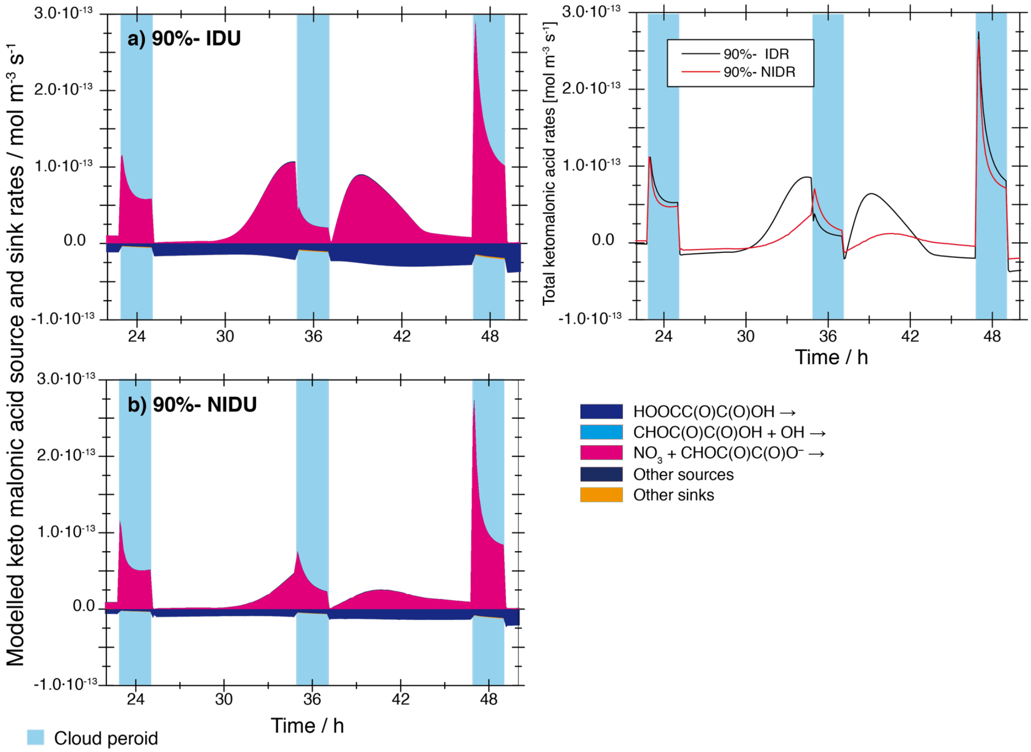

Figure S2 Modelled chemical sink and source mass rates of keto malonic acid in the aqueous phase in mol m^{-3} s^{-1} for the second day of modelling time for the urban scenarios, 90 %-IDU vs. 90 %-NIDU. a) Ideal solutions (90 %-IDU), b) non-ideal solutions (90 %-NIDU).

Supplement S2: Figures

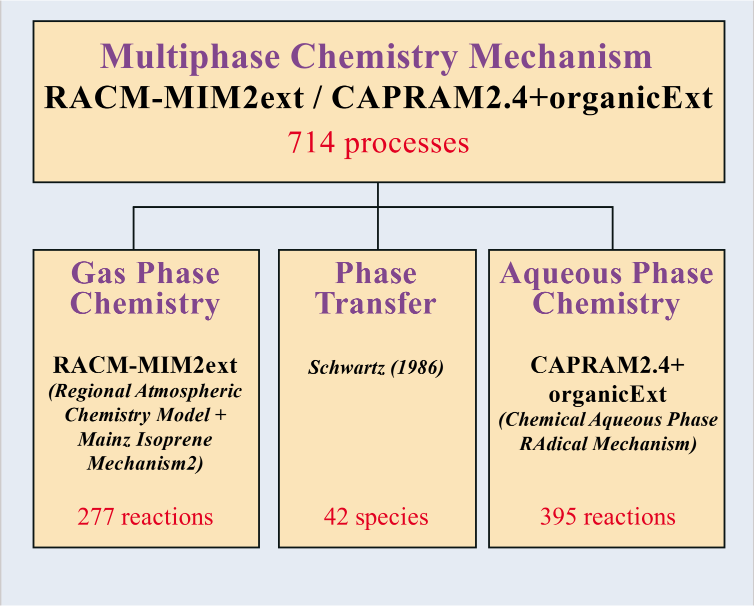

Figure S3. Schematic of multiphase mechanism employed in this study, including the number of processes, reactions, and phase transfer processes (modified from Deguillaume et al. (2009); Tilgner and Herrmann (2010)).

Additional model results of the remote and urban simulation cases

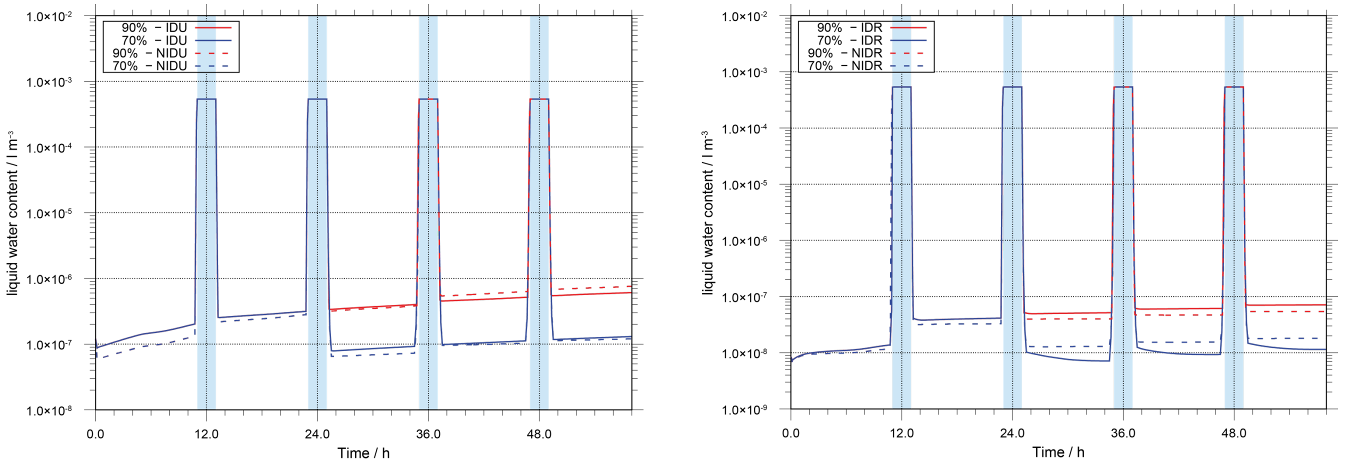

Figure S4. Modelled Liquid Water Content in $\mathrm{l_{(water)}\,m^{-3}{}_{(air)}}$ throughout the simulation time for the different urban (left) and remote (right) simulation cases (90 %-IDR/90 %-NIDR and 70 %-IDR/70 %-NIDR).

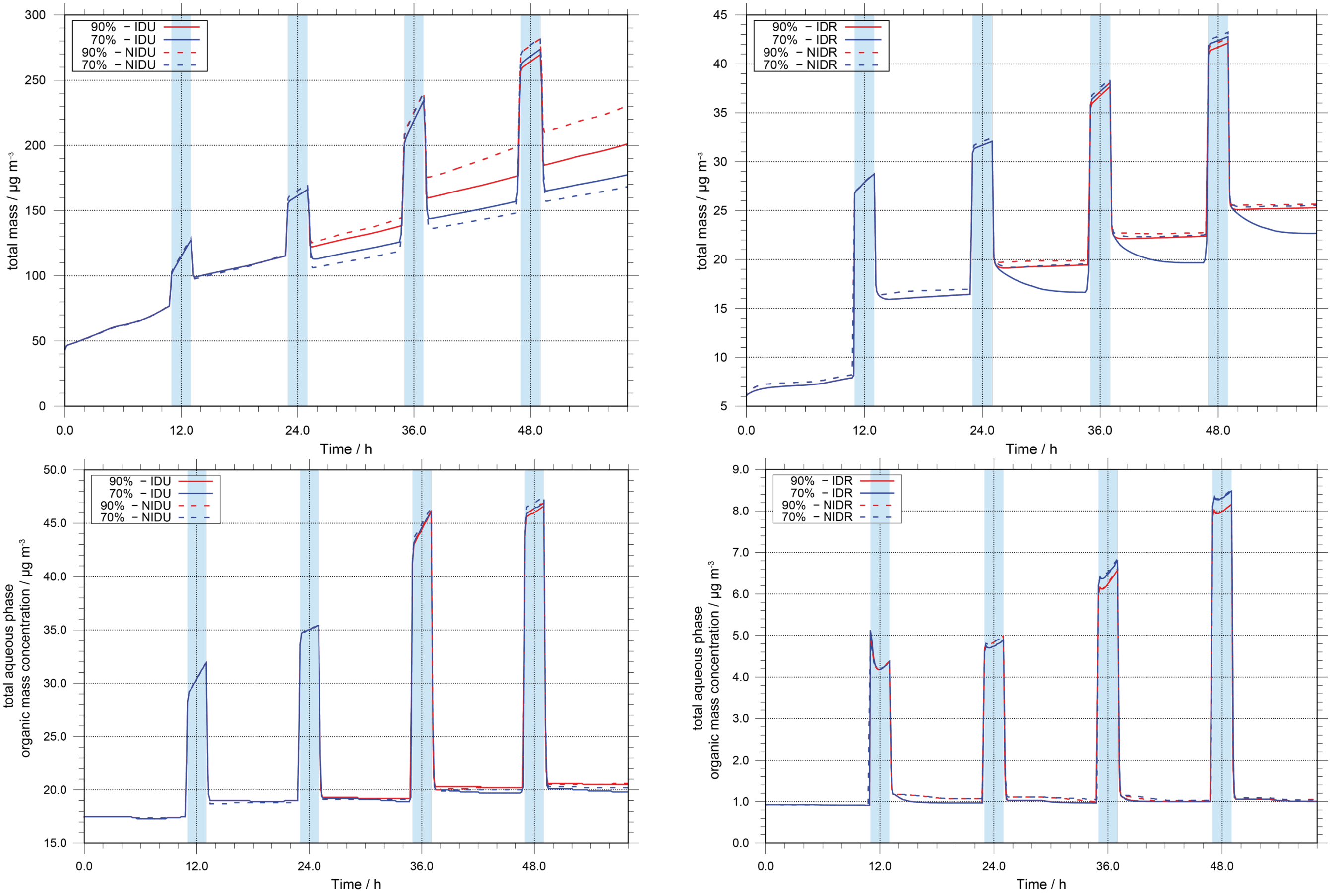

Figure S5. Modelled concentrations in $\mu\mathrm{g\,m^{-3}{}_{(air)}}$ of the total (top), and organic (bottom) aerosol mass throughout the simulation time for the different remote simulation cases (90 %-IDR/90 %-NIDR and 70 %-IDR/70 %-NIDR).

Additional reaction rate analyses plots

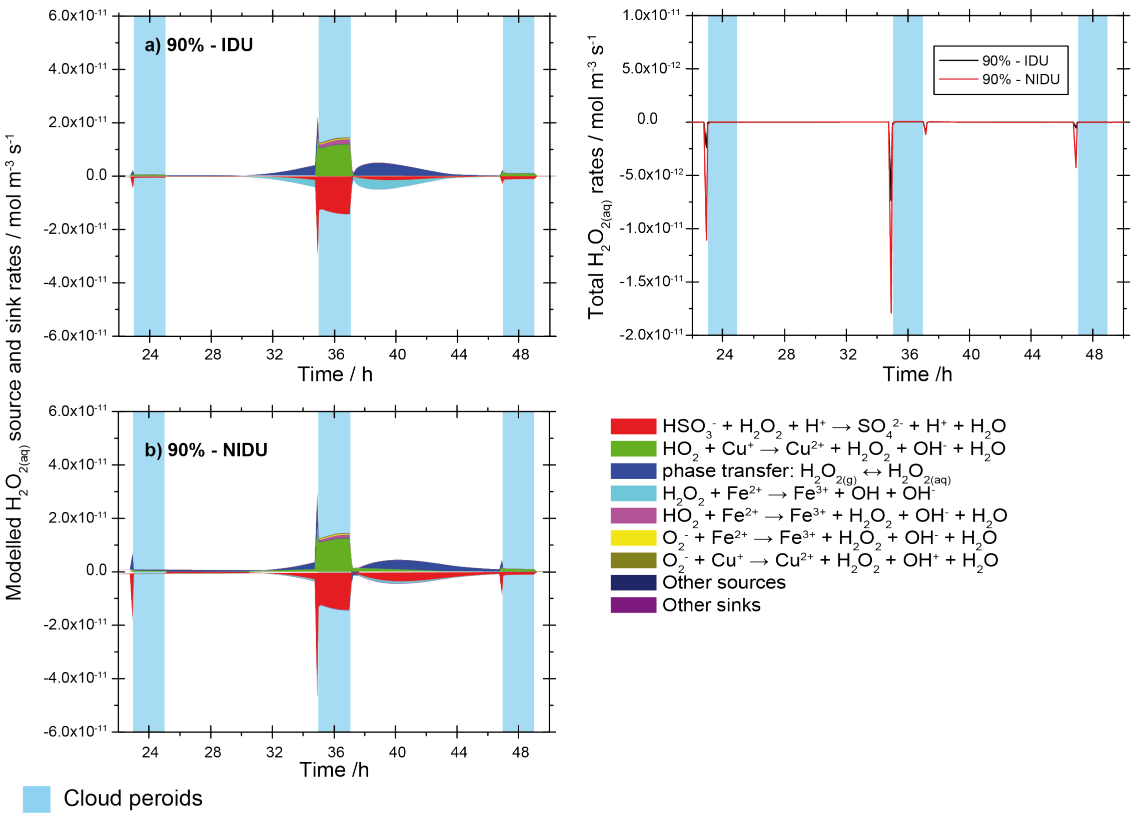

Figure S6 Modelled chemical sink and source mass rates of H_2O_2 in the aqueous phase in mol m^{-3} s^{-1} for the second day of modelling time for the urban scenario for the simulations 90 %-IDU vs. 90 %-NIDU. a) Ideal solutions (90 %-IDU), b) non-ideal solutions (90 %-NIDU), c) corresponding total rates.

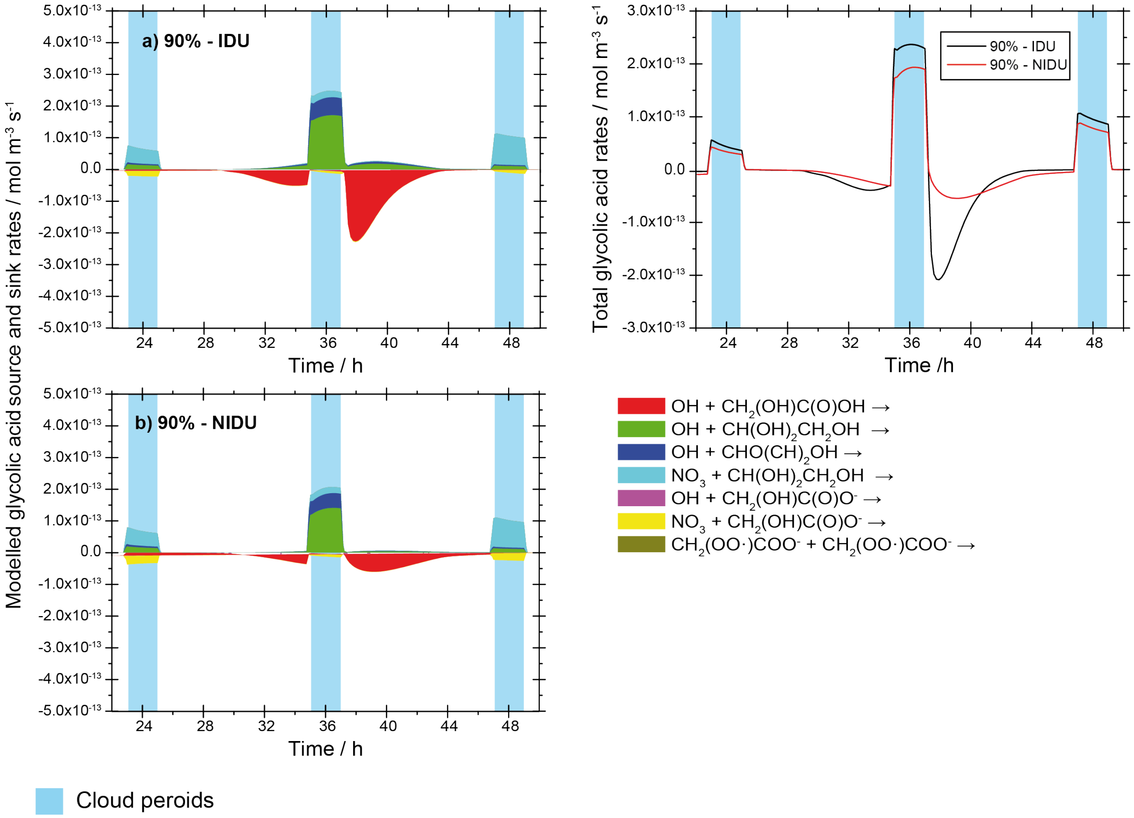

Figure S7 Modelled chemical sink and source mass rates of glycolic acid in the aqueous phase in mol m^{-3} s^{-1} for the second day of modelling time for the urban scenario for the simulations 90 %-IDU vs. 90 %-NIDU. a) Ideal solutions (90 %-IDU), b) non-ideal solutions (90 %-NIDU), c) corresponding total rates.

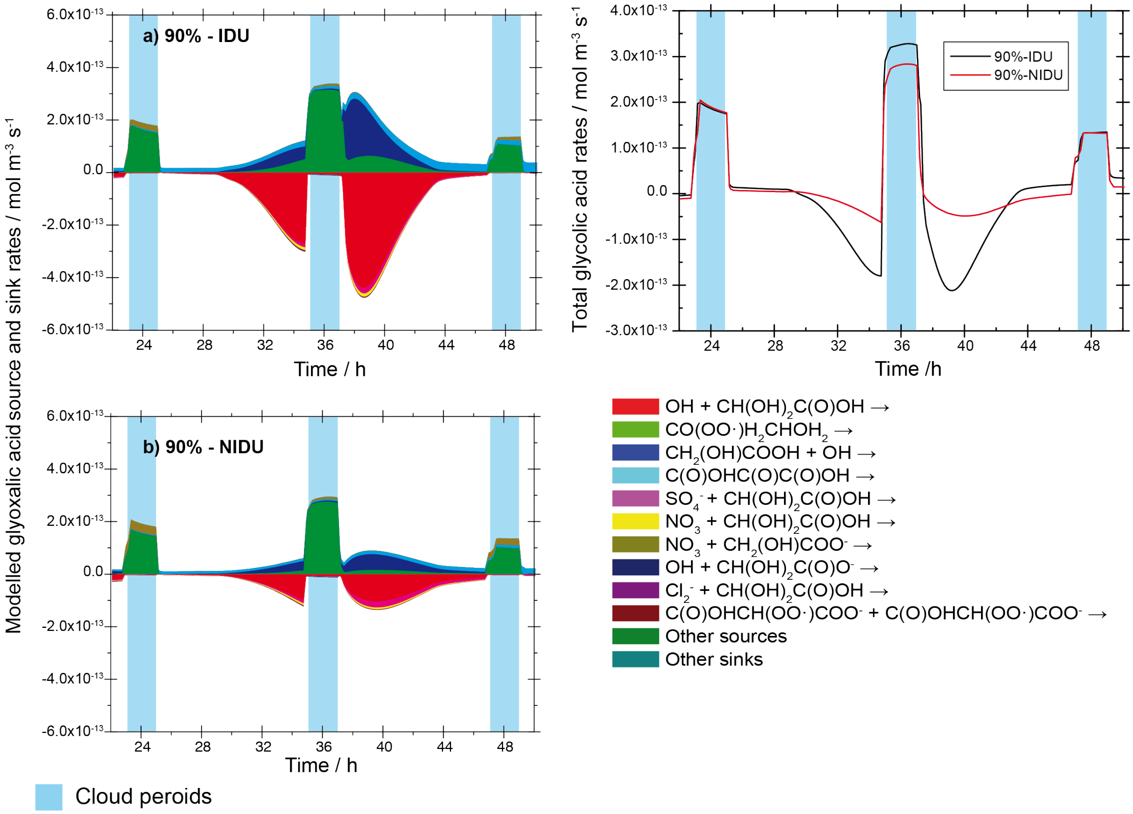

Figure S8 Modelled chemical sink and source mass rates of glyoxylic acid in the aqueous phase in mol m^{-3} s^{-1} for the second day of modelling time for the urban scenario for the simulations 90 %-IDU vs. 90 %-NIDU. a) Ideal solutions (90 %-IDU), b) non-ideal solutions (90 %-NIDU), c) corresponding total rates.

Model results of the remote simulation cases

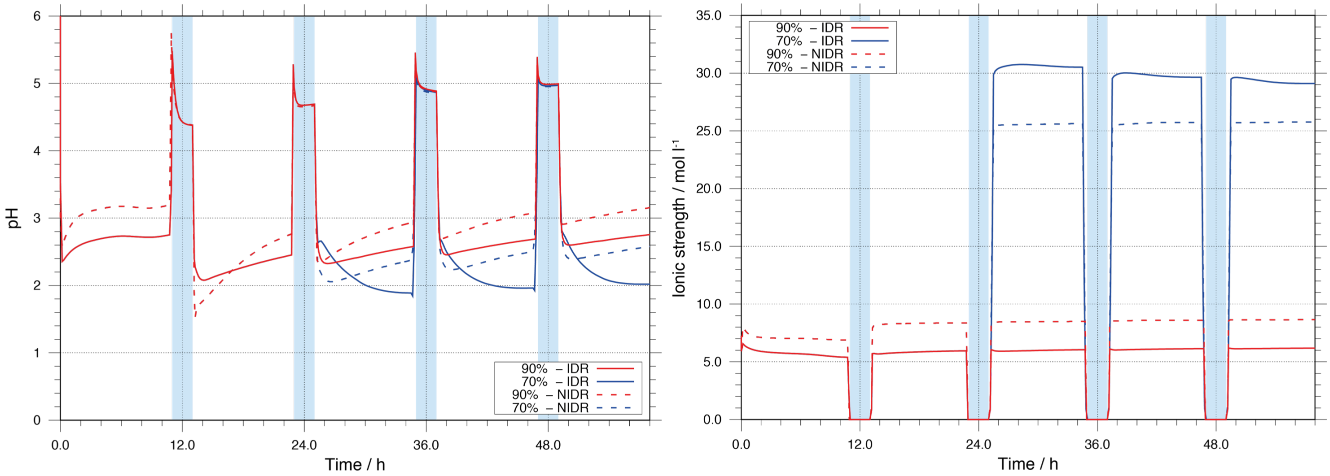

Figure S9. Modelled pH value (left) and ionic strength (I, right) as a function of simulation time for the different remote simulation cases (90 %-IDR/90 %-NIDR and 70 %-IDR/70 %-NIDR).

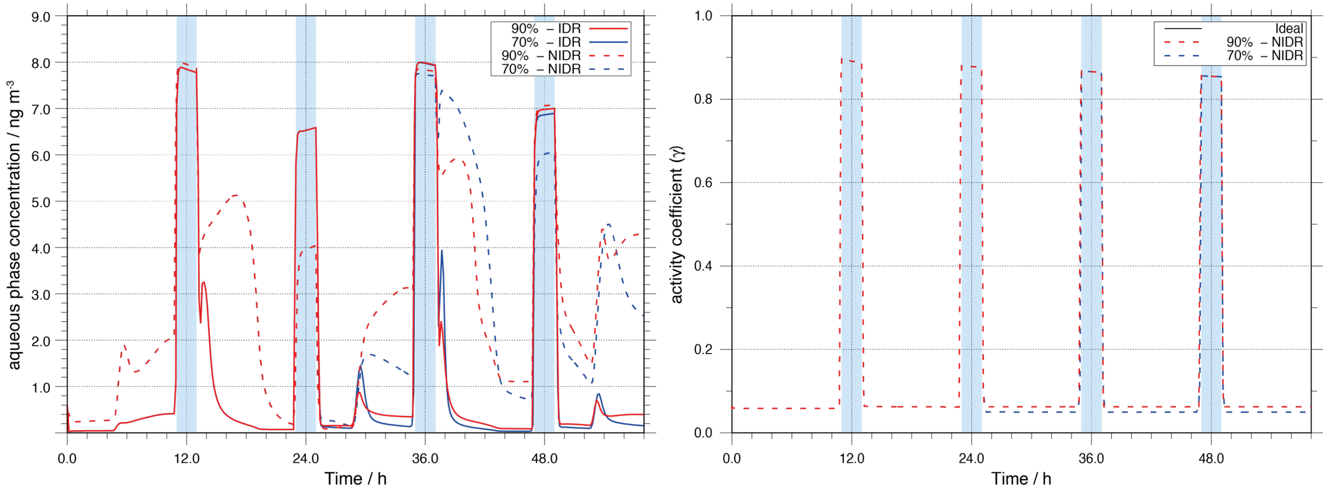

Figure S10. Modelled Fe(II) aqueous-phase concentration in ng m^{-3} throughout the modelling time (left) and corresponding time evolution of activity coefficients (right) for the different remote simulation cases (90 %-IDR/90 %-NIDR and 70 %-IDR/70 %-NIDR).

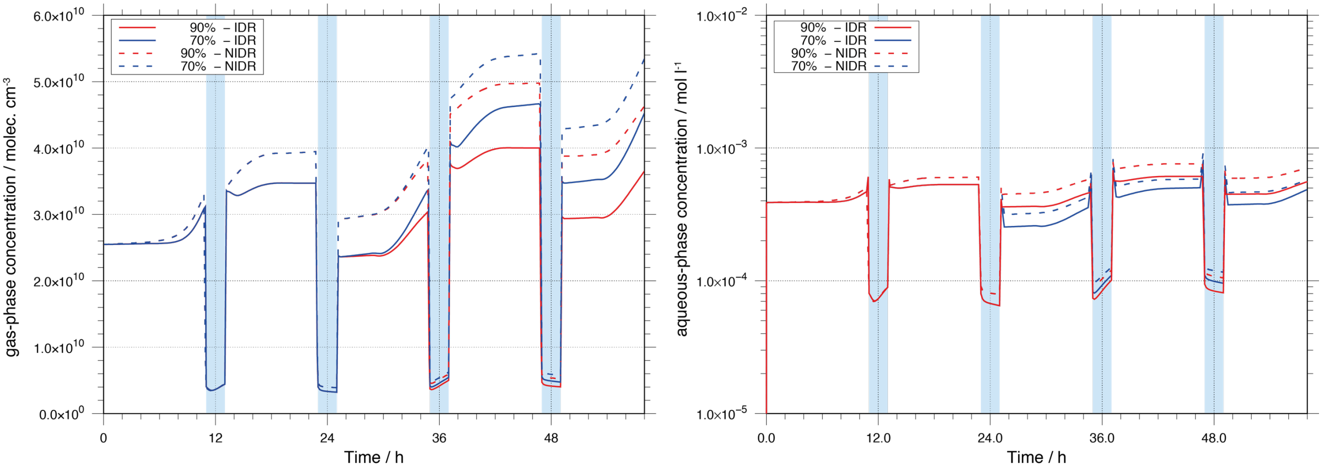

Figure S11. Modelled gas- and aqueous-phase concentration of H_2O_2 throughout the simulation time for the different remote simulation cases (90 %-IDR/90 %-NIDR and 70 %-IDR/70 %-NIDR).

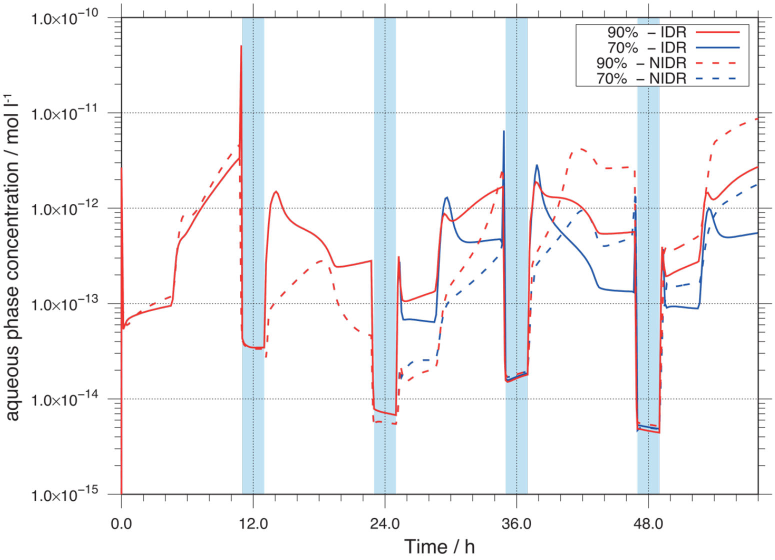

Figure S12. Modelled aqueous-phase OH concentration in mol l^{-1} throughout the simulation time for the different remote simulation cases (90 %-IDR/90 %-NIDR and 70 %-IDR/70 %-NIDR).

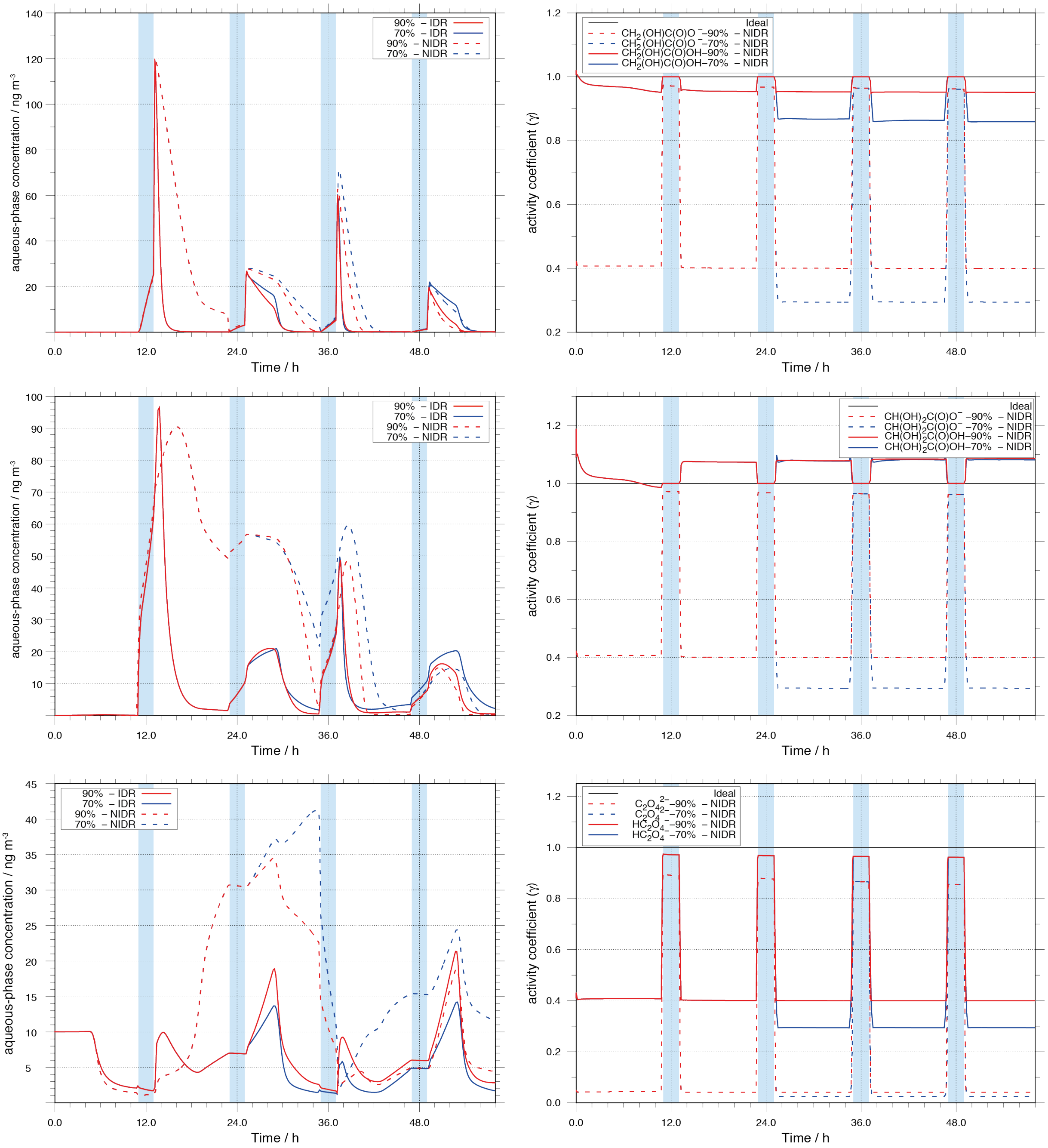

Figure S13. Modelled aqueous-phase concentrations in $\text{ng m}^{-3}_{(\text{air})}$ and corresponding activity coefficients for important C_2 oxidation products, (i) glycolic acid (top), (ii) glyoxylic acid (centre), and (iii) oxalic acid (down) throughout the simulation time for the different remote simulation cases (90 %-IDR/90 %-NIDR and 70 %-IDR/70 %-NIDR). The plotted concentrations represent the sum of dissociated and undissociated forms of the carboxylic acids.

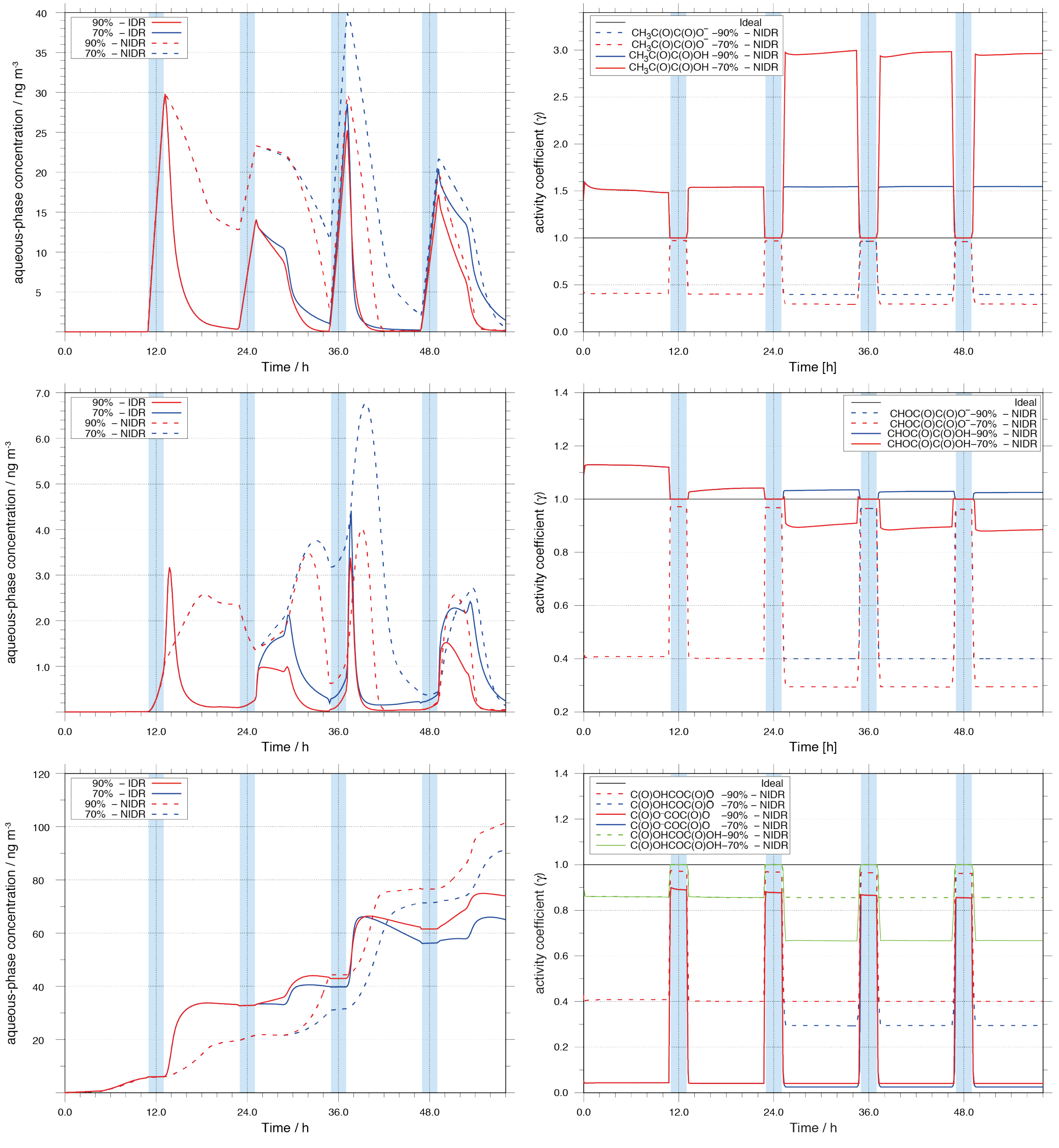

Figure S14. Modelled aqueous-phase concentrations in ng m$^{-3}{}_{(air)}$ and corresponding activity coefficients for important C_3 oxidation products, (i) pyruvic acid (top), (ii) 3-oxo-pyruvic acid (centre), and (iii) keto malonic acid (down) throughout the simulation time for the different remote simulation cases (90 %-IDR/90 %-NIDR and 70 %-IDR/70 %-NIDR). The plotted concentrations represent the sum of dissociated and undissociated forms of the carboxylic acids.

Supplement S3: Additional sensitivity runs

In order to study, the sensitivity of the model with regards to missing middle-range (MR) interaction parameters, additional sensitivity simulations have been performed (acronyms: 90/70% NIDU/NIDR (MR)). For the sensitivity simulations, the MR interaction parameters of Cu^{2+} has been applied for Fe^{2+}/Mn^{2+}. As there are no MR interaction parameters for triply charged transition metal ions available, no MR values are applied for those transition metal ions. However, since particularly Fe^{2+} is the key transition metal ion for the overall TMI processing, the performed sensitivity studies reveal the potential effects of an improved description of the MR interaction parameters.

In Fig. S13 and S14, simulation results of non-ideal runs with and without considered MR interaction parameters are shown for key chemical substances that are sensitive to a non-ideal treatment under remote and urban conditions. The consideration of MR interaction parameters for Fe^{2+}/Mn^{2+} leads to similar activity coefficient pattern for Cu^{2+} and Fe^{2+}/Mn^{2+} (cp. Fig. S15). In comparison to base run without the MR parameters, the activity coefficient values of Fe^{2+}/Mn^{2+} significantly higher and even above 1 under 70% RH conditions as observed for Cu^{2+}. Particularly, the higher activity coefficient values of Fe^{2+} in the MR-cases significantly affects key chemical subsystems (cp. Fig. S16 and S17). For H_2O_2, the model results show that the consideration of MR parameters leads to lower concentrations levels due to more effective loss processes such as the Fenton chemistry. As a consequence, the aqueous OH concentrations are significantly raised and slightly higher oxalic acid concentrations are modelled indicating a more effective organic acid formation as a result of the higher OH levels. On the other hand, the effects on the S(VI) formations are relatively small and only present in the urban simulations.

Because of the higher activity coefficient under consideration of MR parameters, the model results shift at least to a certain part towards the simulations without non-ideal chemistry treatment with a more active TMI-HOx cycling under deliquesced aerosol conditions. Overall, the sensitivity studies clearly show that middle-range (MR) interaction parameters of key TMIs represents crucial parameter that need to be determined in future laboratory experiments to improve current model implementations.

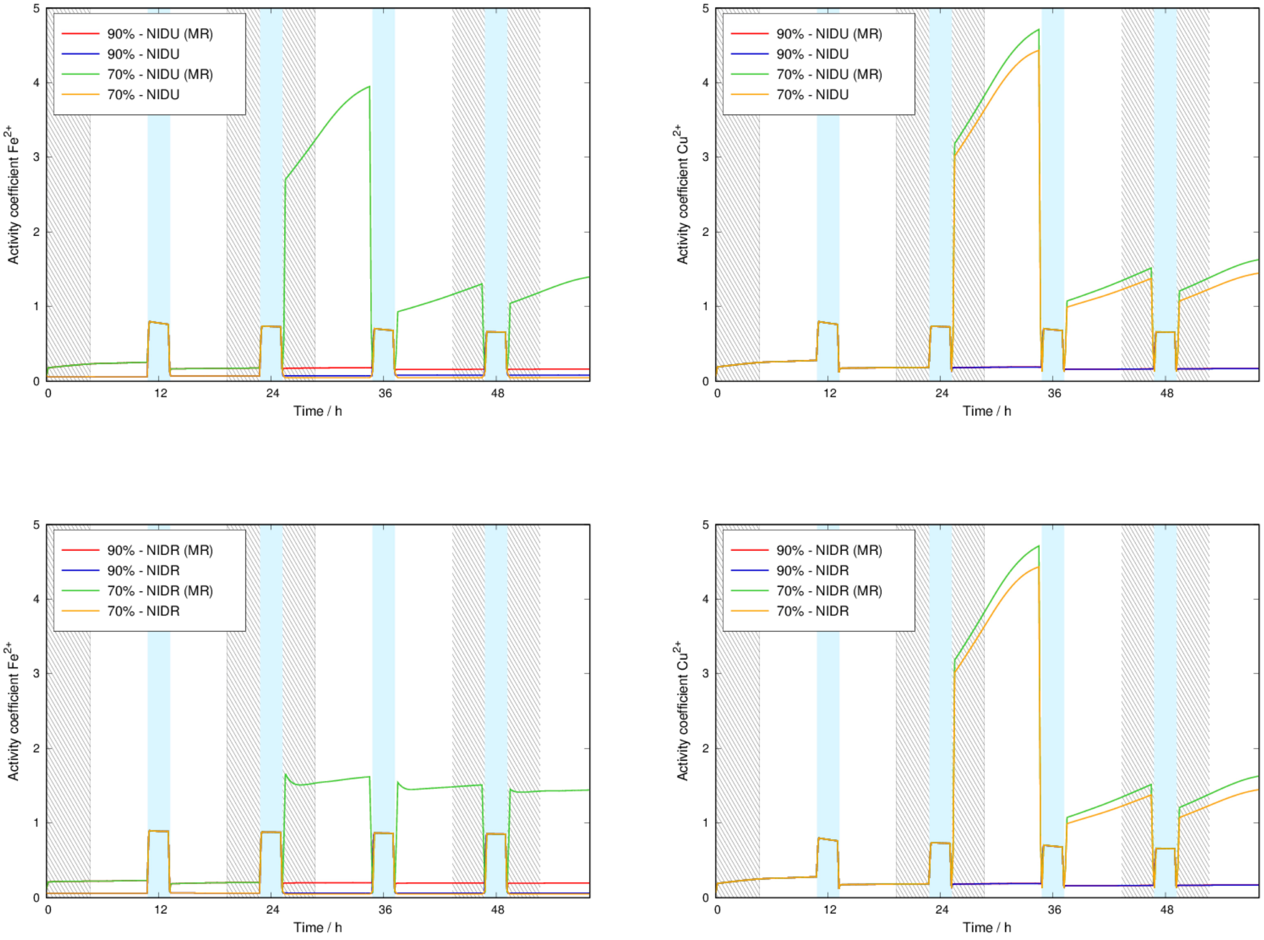

Figure S15. Modelled activity coefficients of Fe^{2+} (left) and Cu^{2+} (right) with and without considered MR parameters for the different non-ideal urban (top) and remote (bottom) model cases.

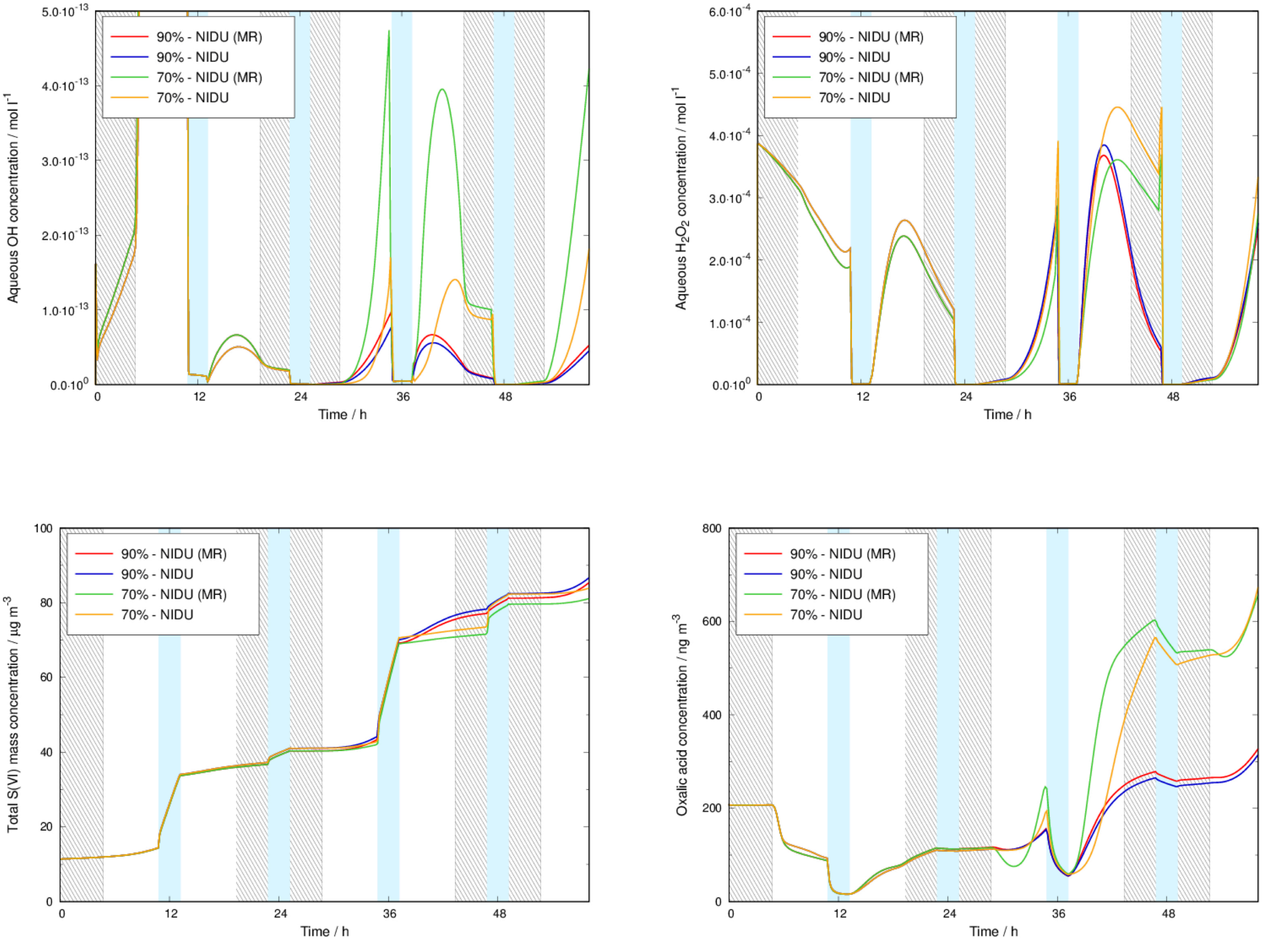

Figure S16. Modelled aqueous-phase concentrations of aqueous OH radical (top left), H_2O_2 (top right), sulfur(VI) (bottom left) and oxalic acid (bottom right) with and without considered MR parameters for the different non-ideal urban model cases.

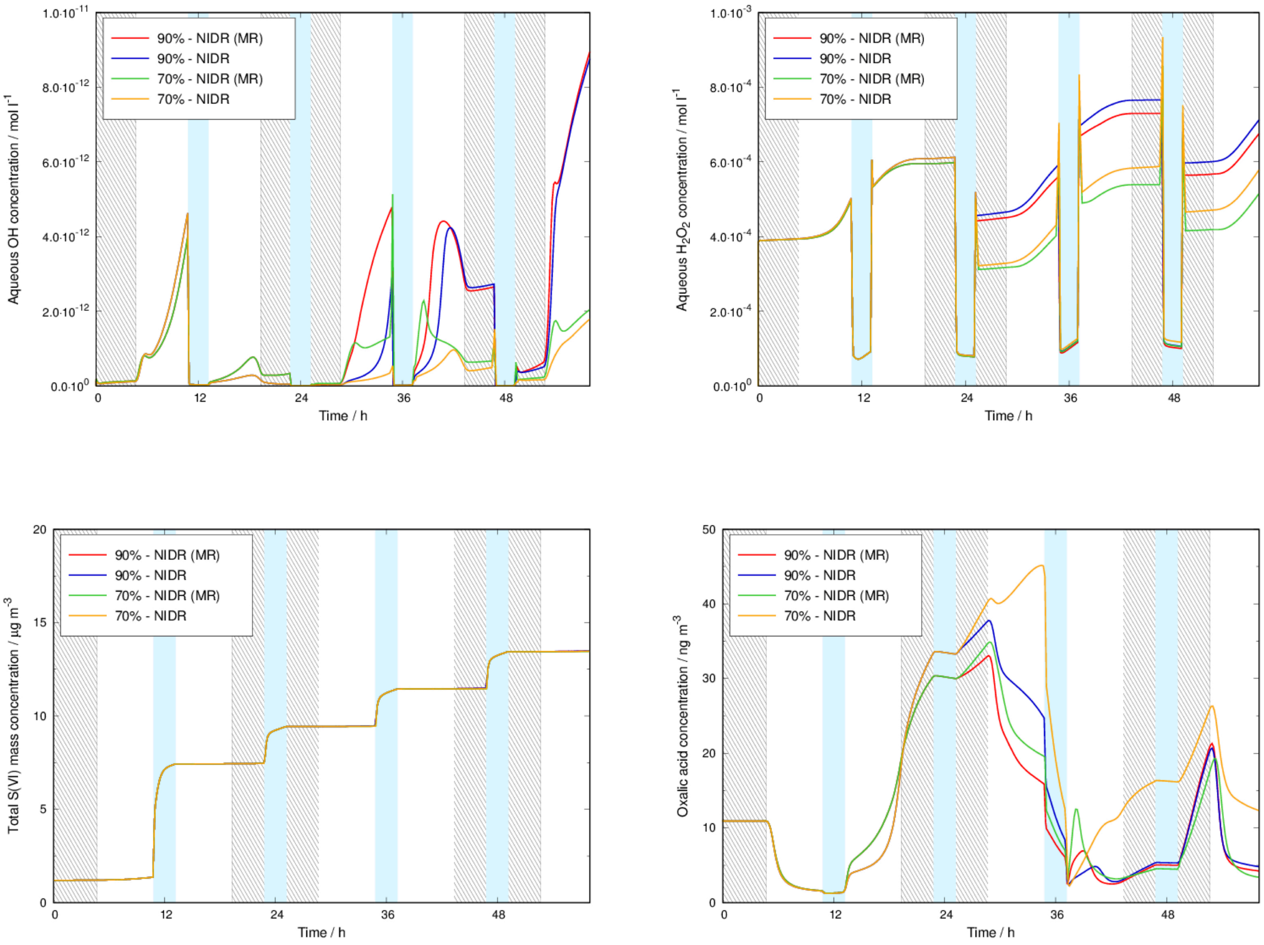

Figure S17. Modelled aqueous-phase concentrations of aqueous OH radical (top left), H_2O_2 (top right), sulfur(VI) (bottom left) and oxalic acid (bottom right) with and without considered MR parameters for the different non-ideal remote model cases.

Supplement S4: Tables

Table S1. Initial chemical aerosol particle composition (relative contributions to the total particulate non-water mass) for the urban and remote environmental model scenarios.

Compound	Urban	Remote
NH_4^+	1.00E-01	9.80E-02
NO_3^-	2.49E-02	9.27E-02
SO_4^{2-}	2.61E-01	1.91E-01
Cl^-	1.92E-02	9.70E-05
Br^-	6.53E-04	1.77E-04
I^-	1.23E-04	1.52E-07
Mn^{3+}	1.54E-04	1.15E-04
Fe^{3+}	1.46E-03	1.42E-03
Cu^{2+}	1.53E-04	1.08E-04
WSOM	1.51E-01	5.57E-02
$HC_2O_4^-$	4.38E-03	1.62E-03
$HOOCCH_2COO^-$	2.79E-03	1.03E-03
$HOOCC_2H_4COO^-$	1.59E-03	5.89E-04
WISOM	2.39E-01	8.83E-02
EC	1.56E-02	1.67E-01
Other anions	7.96E-05	1.89E-04
Cations (+)	3.26E-02	1.53E-02
Cations (2+)	1.49E-02	1.85E-02
Other metals	3.25E-02	4.05E-02
SiO2	9.53E-02	2.27E-01
P	2.87E-03	2.73E-04

Remarks: Single species and compound groups marked in italics are treated in SPACCIM as non-reactive species. The respective ions are just considered for the charge balance.

Table S2. Parameters (N: Number, ρ: Density, r: Radius) of the mono-disperse aerosol particle initialisation for the urban and remote environmental model scenarios.

Parameter	Urban	Remote
N (#/cm^3)	7.0E+08	1.0E+08
ρ (kg/m^3)	1770	1770
r (m)	2.0E+07	2.0E+07

References

Deguillaume, L., Tilgner, A., Schrödner, R., Wolke, R., Chaumerliac, N., and Herrmann, H.: Towards an operational aqueous phase chemistry mechanism for regional chemistry-transport models: CAPRAM-RED and its application to the COSMO-MUSCAT model, J. Atmos. Chem., 64, 1-35, doi:10.1007/s10874-010-9168-8, 2009.

Tilgner, A., and Herrmann, H.: Radical-driven carbonyl-to-acid conversion and acid degradation in tropospheric aqueous systems studied by CAPRAM, Atmos. Environ., 44, 5415-5422, doi:10.1016/j.atmosenv.2010.07.050, 2010.